Orbitals for classical arbitrary anisotropic colloidal potentials

Martin Girard, Trung Dac Nguyen, and Monica Olvera de la Cruz*
Department of Materials Science and Engineering, Northwestern University, Evanston, Illinois 60208, USA
(Received 5 September 2017; published 20 November 2017)

Coarse-grained potentials are ubiquitous in mesoscale simulations. While various methods to compute effective interactions for spherically symmetric particles exist, anisotropic interactions are seldom used, due to their complexity. Here we describe a general formulation, based on a spatial decomposition of the density fields around the particles, akin to atomic orbitals. We show that anisotropic potentials can be efficiently computed in numerical simulations using Fourier-based methods. We validate the field formulation and characterize its computational efficiency with a system of colloids that have Gaussian surface charge distributions. We also investigate the phase behavior of charged Janus colloids immersed in screened media, with screening lengths comparable to the colloid size. The system shows rich behaviors, exhibiting vapor, liquid, gel, and crystalline morphologies, depending on temperature and screening length. The crystalline phase only appears for symmetric Janus particles. For very short screening lengths, the system undergoes a direct transition from a vapor to a crystal on cooling; while, for longer screening lengths, a vapor-liquid-crystal transition is observed. The proposed formulation can be extended to model force fields that are time or orientation dependent, such as those in systems of polymer-grafted particles and magnetic colloids.

DOI: 10.1103/PhysRevE.96.053309

I. INTRODUCTION

Efforts to synthesize and assemble anisotropic particles such as Janus particles [1–5], patchy colloids [6,7], polyhedral particles [8], and functionalized polyhedral nanoparticles [9] have led to materials with diverse structures and functionalities. Systems described by and modeled on anisotropic interactions also include proteins [10–13] and polyhedral colloids [14–17]. The anisotropy of the interaction field is akin to that of the electron orbitals of individual atoms or molecules and could enhance control of structural properties such as that of the crystal lattices formed [9,13].

Simulations can guide experimental attempts to self-assemble systems with anisotropic interactions. While state-of-the-art simulations are often effective at both the micro (particle-based description) and macro (continuum) scales, they frequently fail at the mesoscopic scale, where macroscopic equations become invalid and the number of particles is too large for efficient computation. Coarse-graining circumvents this problem by reducing the number of degrees of freedom. For instance, the interactions of spherical colloids are generally rewritten as a function of the distance between the spheres only, discarding fine details such as surface roughness and the explicit nature of grafted chemical components. For nonspherical colloids of arbitrary nature, one must take into account the relative orientation of the colloids. The single degree of freedom for two spherically symmetric colloids then becomes six degrees of freedom.

All-atom molecular force fields encounter similar problems for rigid molecules, where fast calculation of interaction potentials is sought [18]. An expansion into spherical harmonics for potentials of the form r^{-a} was explored, which yields products of spherical harmonics and hypergeometric functions. Sack attacked the problem of arbitrary interactions between sites [19] but could not obtain any explicit form. Ruedenberg used properties of Fourier transforms to reformulate the problem as an integral representation [20]; however, in numerical implementations, calculating hypergeometric functions is prohibitively expensive. A few other approaches that do not involve spherical harmonics have been attempted, such as expressing excluded-volume interactions in liquid crystals using the Gay-Berne potential and subsequent refinements [21,22] and using potential decomposition for lock-and-key systems [23]. However, a general description of arbitrary potentials remains elusive. The common solution is to use brute-force calculation, where the surface is tessellated with particles and some not necessarily physical interaction is used between surface particles.

Here, we revisit this problem for the general case of arbitrary bodies. We expand interactions into orbital-like interactions which are efficiently evaluated by Fourier transforms in the spirit of Ruedenberg [20]. Previous approaches aimed at obtaining analytical formulations require solving an integral and evaluating computationally expensive functions. We avoid explicitly computing these integrals by relying on tabulations of Fourier integrals and their full derivatives. Our approach is equivalent to *ab initio* molecular dynamics (AIMD), where the amplitudes are replaced by densities [24]. The numerical implementation avoids the Pulay forces which plague traditional AIMD. This orbital expansion is truncated at some appropriate level, which effectively smooths the particle description and produces expressions closely related to classical multipole expansions. We implement this potential in the LAMMPS software package [25] and provide a simple implementation for the uniaxial case (see Supplemental Material [26] for implementation details).

The method requires two conditions: (1) that the orbital expansion of a particle is time invariant (that is, the particle shape does not change over time), which is a reasonable approximation for colloids grafted with a very dense brush and for rigid bodies with charges on the surface, and (2) that the interaction potential possesses a Fourier transform. A large set of potentials satisfy this second requirement, including

*m-olvera@northwestern.edu

Coulomb, Yukawa, and Gaussian potentials; whereas the well-known Lennard-Jones potential does not, due to its rapidly divergent excluded volume term at $r = 0$. Excluded volume interactions can be resolved, for example, by using a Gaussian force, a technique used in mean-field theories [27–29].

We first introduce the method and a numerical implementation (Sec. II). We derive the field representation for a system of colloids interacting through a Gaussian surface charge distribution and for a system of charged Janus particles in a screened environment. For the Gaussian charged particles, for which the multipole expansion terminates, we show that this method is exact and thus has improved accuracy compared with a naive tessellation of the surface (Sec. III A). For the charged Janus particles (Sec. III B), which was previously examined using a Kern-Frenkel potential valid only at very short screening lengths [30], we extend the calculation to higher screening lengths, which is a regime typically difficult to access numerically. The limitations of the method are also discussed (Sec. III C).

II. FIELD REPRESENTATION OF PAIRWISE POTENTIALS

A. Motivating example

Consider a system of charged particles interacting through a screened Yukawa potential. We assume that particle i is located at $\vec{r}_i$ with orientation $\hat{R}_i$. Let $\rho(\vec{r},\hat{R})$ be the distribution of interacting particles and $\chi(r)$ their interaction potential. $\chi(r)$ must possess a Fourier transform; otherwise, it has no restriction. In the case of charged particles interacting through a Yukawa potential, $\rho_i(\vec{r}-\vec{r}_i,\hat{R}_i)$ is the charge distribution and $\chi_{\rm es}(r) = r^{-1}\exp(-\kappa r)$. The interaction is given by the integral:

$$U^{\rm es}_{ij}(\vec{r}_i,\hat{R}_i,\vec{r}_j,\hat{R}_j) = \int_V \rho_i(\vec{r},\hat{R}_i)d\vec{r}\int_{V'}\chi_{\rm es}(|(\vec{r}-\vec{r}\,'-\vec{r}_{ij}|)\rho_j(\vec{r}\,',\hat{R}_j)d\vec{r}\,', \quad (1)$$

where $\vec{r}_{ij} = \vec{r}_j - \vec{r}_i$ and the coordinates are centered around the two colloids i and j. The second integral in Eq. (1) is a convolution of ρ_j with $\chi_{\rm es}$, which we introduce as the auxiliary field Φ_ρ,

$$\Phi_{\rho_j}(\vec{r},\hat{R}_j) = \int_{V'}\chi_{\rm es}(|\vec{r}-\vec{r}\,'|)\rho_j(\vec{r}\,',\hat{R}_j)d\vec{r}\,' = \rho_j(\vec{r},\hat{R}_j) * \chi_{\rm es}(r), \quad (2)$$

where $*$ denotes the convolution operation. The electrostatic potential energy between the colloids is then rewritten as the overlap integral of the auxiliary field with the density field as:

$$U^{\rm es}_{ij}(\vec{r}_i,\hat{R}_i,\vec{r}_j,\hat{R}_j) = \int_V \rho_i(\vec{r}-\vec{r}_i,\hat{R}_i)\Phi_{\rho_j}(\vec{r}-\vec{r}_j,\hat{R}_j)d\vec{r}, \quad (3)$$

where we expanded the auxiliary field around the center of the colloid j for symmetry considerations that will become clear later. While the density $\rho(\vec{r},\hat{R})$ and interaction $\chi(r)$ fields are scalar, generalization to tensor fields is straightforward, as shown for the vector case in Appendix C.

B. Field equations

We now derive the general formalism for forces based on overlaps of fields. We consider two arbitrary fields $\Phi_i(\vec{r}-\vec{r}_i,\hat{R}_i)$ located near colloid i and $\Phi_j(\vec{r}-\vec{r}_j,\hat{R}_j)$ located near colloid j as we did in the previous section. In the case of electrostatic interactions, $\Phi_i(\vec{r}-\vec{r}_i,\hat{R}_i) = \rho_i(\vec{r}-\vec{r}_i,\hat{R}_i)$ and $\Phi_j(\vec{r}-\vec{r}_j,\hat{R}_j) = \Phi_{\rho_j}(\vec{r}-\vec{r}_j,\hat{R}_j) = [\rho_j(\vec{r}-\vec{r}_j,\hat{R}_j) * \chi_{\rm es}(r)]$. The overlap integral in which we are interested is given by

$$U_{ij}(\vec{r}_i,\hat{R}_i,\vec{r}_j,\hat{R}_j) = \int_V \Phi_i(\vec{r}-\vec{r}_i,\hat{R}_i)\Phi_j(\vec{r}-\vec{r}_j,\hat{R}_j)d\vec{r}. \quad (4)$$

We first rewrite the left-hand side of Eq. (4). Without making any assumptions on the particular shape of each particle or field, we have six degrees of freedom, three for the relative position of the second particle with respect to the first one and three for the rotation of the second particle. To obtain completely symmetric forms suitable for molecular dynamics (MD), we treat the potential energy as having nine degrees of freedom, three for the center to center vector $\vec{r}$, three for the rotation of the first particle, and three for the rotation of the second particle.

Without loss of generality, we can assume that the particle i is located at the origin. We note that Eq. (4) is very similar to the convolution integral treated by Fourier transforms [31]. Denoting the difference in colloid position by $\vec{r}_{ij} = \vec{r}_j - \vec{r}_i$ and geometrical inversion of $f(\vec{r})$ by $\underline{f}(\vec{r})$ such that $\Phi_j(\vec{r}-\vec{r}\,') = \underline{\Phi_j}(\vec{r}\,'-\vec{r})$, we cast Eq. (4) as the convolution of Φ_i and the inversion of Φ_j:

$$U_{ij}(\vec{r}_{ij},\hat{R}_i,\hat{R}_j) = \int_V \Phi(\vec{r})\underline{\Phi_j}(\vec{r}_{ij}-\vec{r})d\vec{r} = \Phi_i(\vec{r}) * \underline{\Phi_j}(\vec{r})|_{\vec{r}=\vec{r}_{ij}}. \quad (5)$$

Within the spherical harmonics transform framework [31], this operation is straightforward in reciprocal space, where $\vec{r}\to\vec{\rho}$, $\Phi(r,\theta,\phi)\to\tilde{\Phi}(\rho,\theta_w,\phi_w)$ is the Fourier transform operation and $\tilde{U}_{ij}(\vec{\rho},\hat{R}_i,\hat{R}_j) = \tilde{\Phi}_i(\vec{\rho},\hat{R}_i)\tilde{\Phi}_j(\vec{\rho},\hat{R}_j)$. We introduce the Wigner functions $\mathcal{D}^l_{m,\mu}(\hat{R})$ to treat the rotation of spherical harmonics, resulting in the full expressions for $\tilde{\Phi}_i$ and $\underline{\tilde{\Phi}_j}$ given by

$$\tilde{\Phi}_i(\vec{\rho}) = \sum_{l_i,m_i,\mu_i}\mathcal{D}^{l_i}_{m_i,\mu_i}(\hat{R}_i)Y^{m_i}_{l_i}(\theta_w,\phi_w)F^{m_i}_{l_i}(\rho), \quad (6)$$

$$\underline{\tilde{\Phi}_j}(\vec{\rho}) = \sum_{l_j,m_j,\mu_j}\mathcal{D}^{l_j}_{m_j,\mu_j}(\hat{R}_j)(-1)^{l_j}Y^{m_j}_{l_j}(\theta_w,\phi_w)F^{m_j}_{l_j}(\rho). \quad (7)$$

The usual spherical harmonics $Y^m_l(\theta,\phi)$ are defined by

$$Y^m_l(\theta,\phi) = \sqrt{\frac{(l-m)!}{(l+m)!}}P^m_l(\cos\theta)\exp(im\phi),$$

where $P^m_l(x)$ is the associated Legendre polynomial of degree l and order m, such that $\int_\Omega Y^m_l(\theta,\phi)Y^{m'}_{l'}(\theta,\phi)d\Omega = \delta_{l,l'}\delta_{m,m'}$. A useful representation of the Wigner $\mathcal{D}^l_{m,\mu}$ function is based on quaternion representation of rotations as developed in

Ref. [32]:

$$\mathcal{D}^{l}_{m,\mu} = \sqrt{\frac{(l+m)!(l-m)!}{(l+\mu)!(l-\mu)!}}|R_a|^{2l-2m}R_a^{m+\mu}R_b^{m-\mu} \times \sum_{\rho}\binom{l+\mu}{\rho}\binom{l-\mu}{l-\rho-m}\left(-\frac{|R_b|^2}{|R_a|^2}\right)^{\rho}, \quad (8)$$

where $R_a = q_w + iq_z$ and $R_b = q_y + iq_x$ and $q = (q_w,\vec{q})$ is a normalized quaternion describing the orientation. The quantities F_l^m are the lth-order spherical Fourier-Bessel transforms of $\Phi(\vec{r})$ given by:

$$F^{m_i}_{l_i} = 4\pi(-i)^{l_i}\int \Phi_i(\vec{r})\overline{Y^{m_i}_{l_i}(\theta,\phi)}j_{l_i}(\rho r)r^2dr, \quad (9)$$

where $j_l(z)$ is the lth-order spherical Bessel function of the first kind. Multiplying Eqs. (6) and (7) and inverting back the transform yields the potential:

$$U_{ij}(\vec{r}_{ij},\hat{R}_i,\hat{R}_j) = \sum_{\substack{l_i,m_i,\mu_i\\ l_j,m_j,\mu_j,L}} 8(-i)^L Y_L^{m_i+m_j}(\theta_{ij},\phi_{ij})\mathcal{D}^{l_i}_{m_i,\mu_i}(\hat{R}_i) \times \mathcal{D}^{l_j}_{m_j,\mu_j}(\hat{R}_j)\mathcal{F}^{m_i,m_j}_{L,l_i,l_j}(r_{ij})\mathcal{C}^{m_i,m_j}_{L,l_i,l_j}, \quad (10)$$

where

$$\mathcal{F}^{m_i,m_j}_{L,l_i,l_j}(r_{ij}) = \left[\frac{i^{l_i+l_j}}{(4\pi)^2}\int_0^\infty F^{m_i}_{l_i}(\rho)F^{m_j}_{l_j}(\rho)j_L(\rho r)\rho^2d\rho\right]_{r=r_{ij}}, \quad (11)$$

$$\mathcal{C}^{m_i,m_j}_{L,l_i,l_j} = \sqrt{\frac{(2l_i+1)(2l_j+1)}{4\pi(2L+1)}}\langle l_i,0,l_j,0,L,0\rangle \times \langle l_i,m_i,l_j,m_j,L,m_i+m_j\rangle \quad (12)$$

and $\langle l_i,m_i,l_j,m_j,L,M\rangle$ is a Clebsh-Gordan coefficient. This definition of $\mathcal{C}^{m_i,m_j}_{L,l_i,l_j}$ is equivalent to the Slater coefficients of Ref. [31]. In the general case, there is no known analytical representation of $\mathcal{F}(r)$, and it must be tabulated.

C. Numerical implementation

The coefficients $\mathcal{F}^{m_i,m_j}_{L,l_i,l_j}(r_{ij})$ are precomputed and compiled into tables. This can be done using known software packages (see provided files) or by fast Fourier-based methods [33]. For Monte Carlo simulations, potential energy given by Eq. (10) is sufficient for sampling. In order to time evolve the system in MD simulations, we must compute forces and torques. In Eq. (10), the position and rotation components are fully decoupled. Forces are given by spatial derivatives, while torques are given by angular derivatives of the Wigner functions. We tabulate the derivative of $\mathcal{F}$ using

$$\frac{\partial\mathcal{F}^{m_i,m_j}_{L,l_i,l_j}}{\partial r} = \frac{i^{l_i+l_j}}{(4\pi^2)}\left\{\int_0^\infty F^{m_i}_{l_i}(\rho)F^{m_j}_{l_j}(\rho) \times \left[\frac{Lj_L(r\rho)}{r} - \rho j_{1+L}(r\rho)\right]\rho^2d\rho\right\}_{r=r_{ij}}. \quad (13)$$

Additional forces arise from the derivatives of the spherical harmonics. Their projection along direction k is calculated by using partial derivatives,

$$F_k \sim \frac{\partial Y_L^M(\theta,\phi)}{\partial\theta}\frac{\partial\theta}{\partial k} + \frac{\partial Y_L^M(\theta,\phi)}{\partial\phi}\frac{\partial\phi}{\partial k}. \quad (14)$$

Partial derivatives of the spherical harmonics are obtained by either multipling by iM or taking the derivative of the associated Legendre polynomial. In practice, since spherical harmonics are polynomials of $\cos(\theta)$, we simply calculate

$$F_k \sim \sqrt{\frac{(l-m)!}{(l+m)!}}\exp(iM\phi)\frac{\partial P_l^m(\cos\theta)}{\partial\cos\theta}\frac{\partial\cos\theta}{\partial k} + iMY_L^M(\theta,\phi)\frac{\partial\phi}{\partial k}. \quad (15)$$

The force can then be computed by addition of all individual contributions. For instance, the $\hat{x}$ component is given by

$$F_x = \frac{\partial\mathcal{F}^{m_i,m_j}_{L,l_i,l_j}}{\partial r}\frac{x}{r} + \frac{\partial U}{\partial\cos\theta}\frac{-2xz}{r^3} + \frac{\partial U}{\partial\phi}\frac{-y}{x^2+y^2}. \quad (16)$$

In order to compute torques, we must take derivatives with respect to infinitesimal rotations along some set of axes. The composition of two rotations, $\hat{R}_1$ and $\hat{R}_2$, with corresponding quaternions q_1 and q_2, is given by the quaternion product q_2q_1. This relation is used to obtain the variation of the quaternion of a particle with respect to a rotation axis. For instance, a rotation along the $\hat{x}$ axis of the referential frame, u_x, will cause a variation in quaternion given by

$$\frac{\partial q}{\partial u_x} = \frac{1}{2}(0,1,0,0)\cdot(q_w,q_x,q_y,q_z). \quad (17)$$

The result is multiplied by the partial derivatives of $\mathcal{D}^{l_j}_{m_j,\mu_j}(\hat{R}_j)$ in order to obtain the full derivative. For instance, the derivative of $\mathcal{D}^{l_j}_{m_j,\mu_j}(\hat{R}_j)$ against a rotation along the axis $\hat{x}$ is given by

$$\frac{\partial\mathcal{D}^{l}_{m,\mu}}{\partial u_x} = \sum_k\frac{\partial D^{l}_{m,\mu}}{\partial q_k}\frac{\partial q_k}{\partial u_x} = -q_x\frac{\partial\mathcal{D}^{l}_{m,\mu}}{\partial q_w} + q_w\frac{\partial\mathcal{D}^{l}_{m,\mu}}{\partial q_x} - q_z\frac{\partial\mathcal{D}^{l}_{m,\mu}}{\partial q_y} + q_y\frac{\partial\mathcal{D}^{l}_{m,\mu}}{\partial q_z}. \quad (18)$$

The Wigner coefficients $\mathcal{D}^{l_j}_{m_j,\mu_j}(\hat{R}_j)$ are calculated directly from quaternions [see Eq. (8)], providing straightforward implementations in MD packages. Since these coefficients and their derivatives are only dependent on individual particle orientations, they are updated once per time step and not for each pair interaction. In principle, one can invert the multiplication order to obtain the torques in the body frame. This removes the μ_i index from the summation in Eq. (10) but requires calculating the Wigner functions once per pair interaction, instead of once per particle. It is not done in the supplied code as it would complicate the LAMMPS implementation without any obvious benefit in computational performance.

D. Gaussian patchy particles

To test the method's accuracy, we consider a case where the series in Eq. (10) terminates and does not require truncation, resulting in a spherical harmonic representation that is exact.

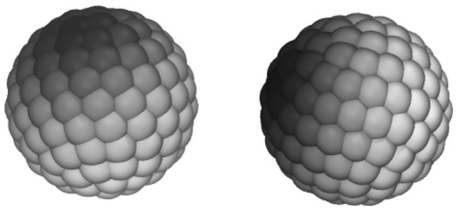

FIG. 1. Representation of the surface function $\rho(S)$ for two interacting particles of arbitrary orientations, where black indicates $\rho = 0$ and white indicates $\rho = 1$.

In particular, we examine colloids with surfaces interacting through a Gaussian potential $\chi_G(r) = a\exp(-br^2)$, where a and b are parameters of the potential. In order for the series to terminate, we use a surface density $\rho_S(\vec{r}) = \delta(|\vec{r}| - 1)(1 + \cos\theta)$, that is, a distribution located on the surface of a particle with radius $R = 1$. The interaction energy between two colloids is written as

$$U_{ij}^{\text{sph}} = a\int \rho_i(S_i)\rho_j(S_j)\exp\left(-br_{S_i,S_j}^2\right)dS_i dS_j, \quad (19)$$

where S_i is the surface of particle i and ρ_{S_i} is a continuous function on the surface of particle i.

We compare the cases where this integral is evaluated using a numerical quadrature with the case where the exact field method is used. Using a numerical quadrature, the integrand is evaluated at N points on each surface, yielding

$$U_{ij}^{\text{sph}} = a(4\pi)^2 N^{-2}\sum_i^N\sum_j^N \rho(\vec{r}_i)\rho(\vec{r}_j) \times \exp(-b|(\vec{r}_i - \vec{r}_j)|^2) + O(N^{-2}). \quad (20)$$

Equation (20) can be directly evaluated in standard MD packages by tessellating the surface of a sphere and assigning charges to each point proportional to $q = (1 + \cos\theta)/N$, where N is the number of points per sphere, as sketched by Fig. 1. The points are chosen according to a Fibonacci mapping in order to obtain an approximately equal area for each point [34]. The interaction between points of the tessellation is taken as $U_{ij}^{\text{tess}} = aq_iq_j\exp(-br^2)$.

For the field representation, the integral in Eq. (4) can be written using the product of two equal fields due to special properties of Gaussian functions (see Appendix B). These two fields are given by $\Phi_i(\vec{r}) = \Phi_G * \rho_i$, where $\Phi_G = a^{1/2}2^{3/2}\pi^{-3/4}b^{3/4}\exp(-2br^2)$, obtained by inverting the square root of the Fourier transform of $\chi_G(r)$. The overall field for this case is then given by

$$\Phi_i(\vec{\rho}) = \Phi_G * \rho_i = \frac{8a^{1/2}\pi^{7/4}\exp\left(-\frac{\rho^2}{8b}\right)}{b^{3/4}} \times\left[\sqrt{\pi}Y_0^0(\theta,\phi)j_0(\rho) + \sqrt{\frac{\pi}{3}}Y_1^0(\theta,\phi)j_1(\rho)\right]. \quad (21)$$

E. Screened Janus particles

Using this method, we can now extend our recent study of charged Janus particles immersed in an ionic solution [30] to the cases where the screening length is on the order of the particle radius. Janus particles possess two sides with equal but opposite charge density. The cap angle, θ_m, dictates the fraction of the surface covered by each charge. This system was previously simulated using a Kern-Frenkel potential, which is valid for very small Debye lengths, that is, $\lambda \ll R$, where λ is the Debye length and R is the particle radius.

In electrostatically screened environments, the coupling is nontrivial. For instance, dipole-dipole and charge-charge interactions generate terms with the same distance dependence [35]. These effects are included in our method.

To calculate interactions between colloids when $\lambda \sim R$, we use Eq. (3). The charge density is given by the following series:

$$\tilde{q}(\vec{\rho}) = -8\pi^{3/2}R^2\left[\cos\theta_m j_0(\rho R)Y_0^0(\theta,\phi) + \sum_{l=1}^{\infty}\sqrt{1+2l}\frac{P_l^1(\cos\theta_m)\sin\theta_m}{l(l+1)}j_l(\rho R)Y_l^0(\theta,\phi)\right]. \quad (22)$$

In reciprocal space, the potential $\chi_{\text{es}}(r)$ is convolved with the charge density by a multiplication using $\tilde{\chi}_{\text{es}}(\rho) = 8\pi^{3/2}(\lambda^{-2} + \rho^2)^{-1}$. The series is truncated at $l_{\max} = 3$ in order to be evaluated numerically and a purely repulsive truncated Lennard-Jones potential (i.e., the Weeks-Chandler-Anderson potential) is added to represent the solid cores of the colloids.

One quickly notices the similarity between Eq. (22) and the usual multipole expansion for charges. A proof of equivalence for $\lambda \to \infty$ is found in Appendix A. Using tabulated integrals over traditional multipoles presents a major advantage since the integral is well-defined in the overlapping regime when $|\vec{r}_{ij}| < R_i + R_j$.

III. RESULTS AND DISCUSSION

A. Accuracy and computational performance

We first characterize the computational efficiency and accuracy of the field respresentation for the Gaussian charged particles. We implement the field representation and the Gaussian charge potential as new force fields in LAMMPS. The benchmark runs are performed with equilibrated systems at similar thermodynamic state points, i.e., number of particles, temperature, and density. LAMMPS is built with the stable 31Mar17 release.

Both the coarse-grained (Gaussian charge) and the spherical harmonic (field) representations achieve strong scaling performance for our numerical implementations, as seen in Fig. 2. The spherical harmonic representation is generally faster than the surface bead representation by a factor of 2.0–3.5, depending on the resolution of the latter. Finer resolution of the surface bead representation increases the computational overhead as N^2, where N is the number of beads discretizing the surface. Furthermore, the spherical harmonic representation exhibits a parallel efficiency as high as 55% at 125 particles per Message Passing Interface (MPI) process. The particularly high parallel efficiency at low particle counts per MPI process, compared to other conventional pairwise potentials (such as Lennard-Jones and Yukawa potentials), implies that the field representation is computationally intensive and thus should further benefit

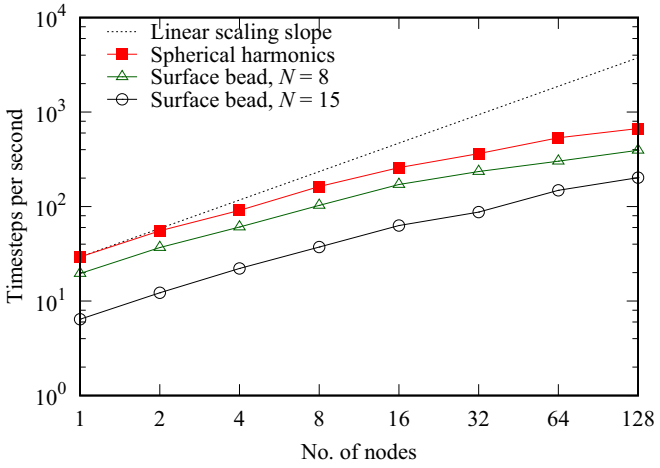

FIG. 2. Strong scaling performance on the Titan XK7 supercomputer. The number of particles in each run is 32 000. There are 16 MPI processes launched on each node.

from finer-grained parallelisms including GPU acceleration, as observed with Gay-Berne potentials [36].

For Gaussian patchy particles, the spherical harmonic representation is exact. Figure 3 compares the average energies of the coarse-grained and field calculations as a function of the number of quadrature points N for a particle with radius $R = 1$ and volume fraction $v \approx 0.077$ using four sets of the potential parameters a,b. The slopes are approximately -2, indicating that the error of the coarse-grained simulation scales as $1/N^2$, consistent with Eq. (20).

Since the calculation speed of the coarse-grained simulations also scales as N^2, accuracy and computational efficiency must be balanced. For this specific system, very few points on the surface are required for accurate simulations. An accuracy of 1% of the mean energy of the system requires approximately 20 beads per surface. Even for this level of precision, however, the spherical harmonic potential method is faster than the

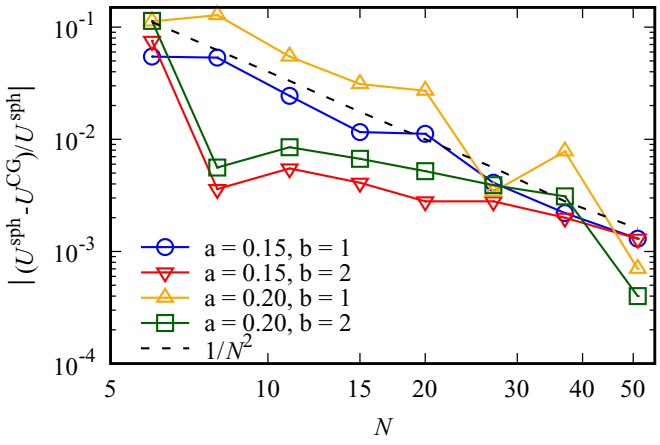

FIG. 3. Relative error of the average energy of the system as a function of the number of tessellation points of the coarse-grained representation. Curves are plotted for $a = (0.15, 0.20)$ and $b = (1, 2)$. The system is in a liquid state with these parameters. An additional curve proportional to $1/N^2$ is drawn for comparison.

coarse-grained representation. The calculation speeds become comparable only when $N \approx 6$–8. Finally, for the $a = 0.2$, $b = 2$, $N = 37$ case, coarse-grained models achieve a calculation speed around 33 time steps per second, compared to 652 time steps per second for the spherical harmonic representation.

B. Janus particles morphologies

To characterize the phase behavior of Janus particles, we simulated particles with two opening angles ($\theta_m = \pi/2$ and $\theta_m = 1.40$) previously calculated using a Kern-Frenkel potential [30]. The simulations were run with 4000 colloids of radius $R = 1$ and a constant volume fraction of $v = 0.10$. The Debye length is varied over the range $0.16 \leqslant \lambda \leqslant 0.32$. The reduced temperature $T^* = \pi\epsilon k_B T R/2q^2$ is varied independently within $1.0 \leqslant T^* \leqslant 2.0$, where ϵ is the permittivity and q is the charge on one of the hemispheres of the balanced $\theta_m = \pi/2$ Janus particle. The system is equilibrated over 3×10^6 time steps. The observed morphologies are summarized in Fig. 4.

For the symmetric Janus particles ($\theta_m = \pi/2$), we observe four morphologies shown in Fig. 5. At very high temperatures, the system is in a vapor phase, labeled V. The system also exhibits a liquid state, labeled L, which seems to correspond to what we previously called a wormlike glass state in Ref. [30]. This liquid phase forms either very small droplets near the V / L boundary or elongated structures. This behavior is similar to that of hard dipole dumbbell systems [37], where it was observed that, while dumbbells with explicit charge or point dipoles exhibit a vapor-liquid transition, point dipole spheres do not [38]. Our simulations suggest that explicit charge representations of spheres also exhibit a vapor-liquid transition.

One should be careful making comparisons between Kern-Frenkel and the present orbital potentials. While they are both approximating the Yukawa potential, it is not the same approximation. Kern-Frenkel assumes that the charge density is locally constant (in a region which size depends on λ). The present orbital representation approximates it using a series. At the opening angle, Kern-Frenkel approximates the mean charge density as either $+1$ or -1 while the orbital gives a sine polynomial dependance. This has strong consequences for crystalline phases, which are very sensitive to the type of interaction used. For instance, crystal formed by colloids interacting through repulsive inverse power laws ($1/r^n$) will exhibit an face-centered cubic (FCC) - body-centered cubic (BCC) transition around an exponent of $n \approx 6$ [39]. Due to these differences, we do not find that the crystal lattice match the previous calculations based on Kern-Frenkel. Nevertheless, the melting temperature of the crystal phase for $\theta_m = \pi/2$, $\lambda = 0.16R$, is around $T^* \approx 0.8$, which is similar to the critical temperature found in the work using the Kern-Frenkel approximation [30], where $T^* = 0.75$.

Interestingly, in the $\theta_m = \pi/2$ case, the liquid morphology only emerges for sufficiently large Debye lengths ($\lambda \gtrsim 0.20$) and sufficiently high temperatures. This phase was absent in our Kern-Frenkel simulations conducted at $\lambda = 0.16$. For very small Debye lengths or very low temperatures, it is replaced by a crystalline morphology. In all observed cases, the system first condenses to the L phase and then crystallizes. Consequently, multiple crystalline domains form on the elongated L structures, instead of single crystals. At large Debye lengths

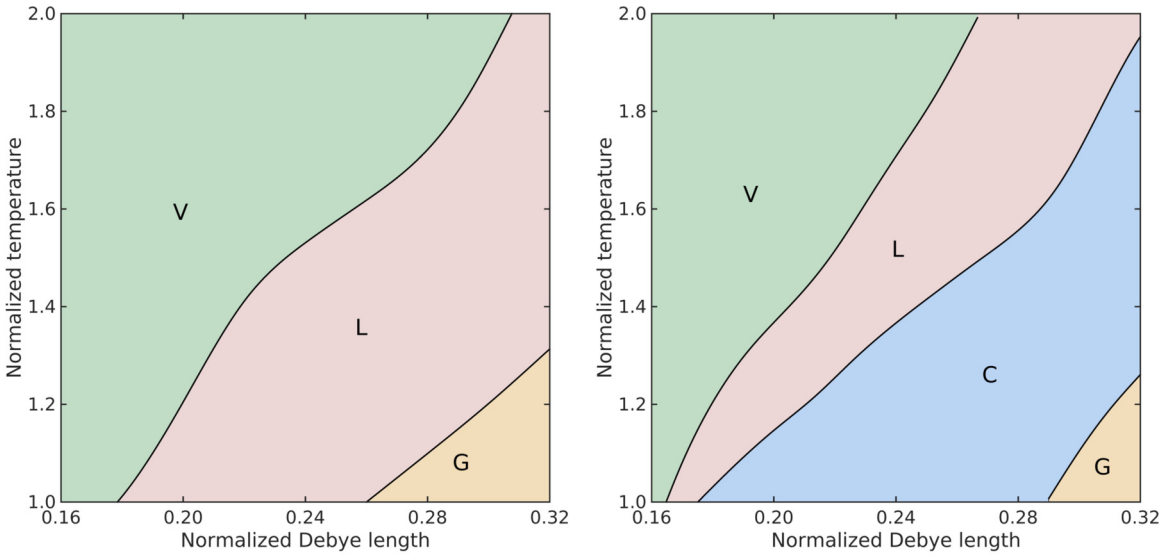

FIG. 4. Regions of observed morphologies in simulations of charged Janus colloids for opening angles of (a) $\theta_m = 1.40$ and (b) $\theta_m = \pi/2$. The different morphologies indicate the main morphology observed. The phase is deemed as vapor by a clustering analysis if more than half the colloids are in clusters of size less than 50. Other morphologies are determined by visual inspection of the trajectories. A morphology is deemed crystalline if it forms at least one crystalline domain. Morphologies are determined for five values of λ and six ($\theta_m = 1.40$) or nine ($\theta_m = \pi/2$) values of temperature, totaling 30 simulated state points for $\theta_m = 1.40$ and 45 for $\theta_m = \pi/2$. Boundaries are obtained by drawing splines in between grid points of different morphologies and should be treated as a guide for the eyes. Coexistence of morphologies is often found along the boundaries.

and low temperatures, the systems starts supporting thinner lines of colloids and the system forms a branched structure, eventually coalescing into a gel-like structure. Whether such a phase is thermodynamically stable or the result of kinetic traps is unknown. However, when $\theta_m = 1.40$ [Fig. 4(a)], the system is liquid near the L/G boundary, which suggests a stable phase. We have performed additional simulations runs at this state point to confirm this hypothesis. More information on the liquid-gel morphology transition can be found in Appendix E.

C. Limitations of the method

As mentioned earlier, the current method has two limitations. First, the interaction potentials χ must possess a Fourier transform. A common source of soft potentials is excluded volumes, which diverge when the volumes overlap. While this is clear from the mathematical equations, the underlying physical reason lies with the fact that series truncation produces a spatial averaging of the densities. This averaging is inconsistent with systems that respond to infinite frequencies. To overcome this limitation, one may be able to represent excluded volumes by expanding Eq. (3) into a summation of integrals of powers of $\rho(\vec{r}, \hat{R})$ or by regularizing the potential function (see Appendix D for further details and derivations).

The second limitation is that density fields must be static in time, which makes the description unsuitable for system with strong deformations. Typical cases include colloids grafted with a low amount of flexible polymers. In such systems, when colloids come close to each other, the polymer coating may deform. In systems of DNA-coated polyhedra, this has been shown to strongly affect broken symmetry regimes, driving transitions between different crystal lattices [9]. These deformations have been the starting point of the orbital topological model, which for polymer coated spheres predicts different equilibrium structures than a regular nondeformable potential [40]. In order to model such a system with our description, one would have to use a time-dependent density field and advance the field over time. We are currently working on such a model, which will be the subject of a future publication.

IV. CONCLUSION

We have developed a field representation for describing the anisotropic interactions between colloids at mesoscopic scales based on an orbital-like decomposition. Using the field representation, several use cases are derived, including patchy particles and charged Janus particles. With this approach, we demonstrate that charge-neutral Janus particles show qualitative agreement with studies of dipolar hard dumbbell systems. Interestingly, the vapor-liquid transition is supplanted by the liquid-crystal transition for very short screening lengths, yielding similar results from the Kern-Frenkel potentials. The liquid phase has previously been shown to be absent for point dipole spheres [38], which raises the question of whether it arises from inclusion of higher-order hexapole terms or disapears at large Debye lengths. Addition of isotropic dispersion forces to systems of point dipole spheres has been shown to cause the liquid phase to appear, provided the dispersion force is sufficiently strong [41]. In our system, the additional hexapole force is entirely determined by the shape of the charges at the surface of the Janus particle. These particles are usually thought of as dipoles and whether the phase diagram can actually be controlled by the surface charge distribution remains an interesting question.

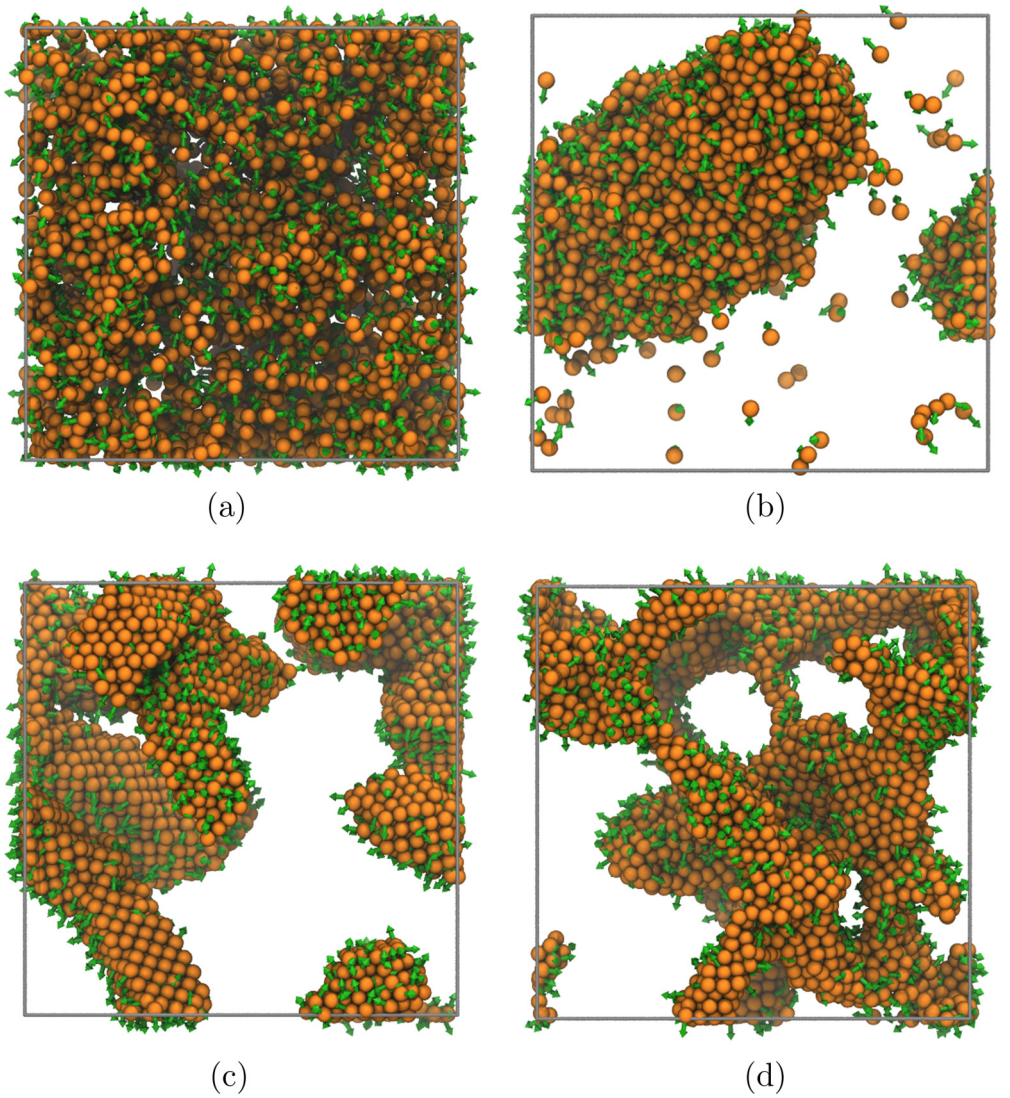

FIG. 5. Snapshots of the simulations in different morphologies observed for symmetric ($\theta_m = \pi/2$) Janus particles: (a) Vapor V state at $T^* = 1.81$, $\lambda = 0.24$; (b) liquid L state at $T^* = 1.50$, $\lambda = 0.24$; (c) crystalline C state at $T^* = 1.20$, $\lambda = 0.24$; and (d) gel state at $T^* = 1.0$, $\lambda = 0.32$. Arrows indicate north pole of the Janus particles.

This technique enables simulations in solutions with screening lengths comparable to the size of the colloids without resorting to expensive and often inaccessible explicit ions simulations. The modest requirements for the type of potentials that can be used make this field coarse-graining approach applicable to many types of interactions. With this flexibility, the technique could potentially be employed to calculate interactions between globular proteins of various shapes and surface compositions stemming from a combination of electrostatics and hydrophobicity. Indeed, our approach has the inherent capability of including position-orientation coupling of particles. It can in principle describe any anisotropic potential, as long as the potential has proper behavior in reciprocal space, and, in the present form, as long as the particles shape and surface composition remain constant as the particles interact.

In order to relax the assumptions made in the present study, namely that the density representing particle shapes is constant and that the surface composition does not change as the particles interact, the field coarse-graining approach has to be extended to directional and time-dependent force fields. While the complexity of the derived field depends on the original interactions and increases with the target accuracy, the performance gain due to finer-grained parallelization can be significant and will be the focus of future studies. A major refinement is to include dynamic densities, which is necessary to efficiently simulate very soft colloids such as polymer-coated particles where the shape of the particle changes when two colloids interact [40]. This refinement is necessary also to make comparison between our approach and results of conventional approaches that include grafted chains such as DNA to nanoparticles explicitly [9].

ACKNOWLEDGMENTS

This work was supported by the Center for Bio-Inspired Energy Science, which is an Energy Frontier Research Center funded by the US Department of Energy, Office of Science, Office of Basic Energy Sciences under Award

No. DE-SC0000989. M.G. acknowledges support from the Natural Sciences and Engineering Research Council of Canada graduate fellowship (Grant No. PGS-D 6799-459278-2014).

APPENDIX A: EQUIVALENCE BETWEEN MULTIPOLE EXPANSIONS

Equation (22) expands the charge into spherical harmonics. Arbitrary rotations of this multipole are treated by Wigner $\mathcal{D}$ functions:

$$\tilde{q}_i(\rho) = -8\pi^{3/2}R_i^2\Bigg[\cos\theta_m j_0(\rho R_i)Y_0^0(\theta,\phi) + \sum_{l=1,m}\mathcal{D}_l^{m,0}(\hat{R}_i) \times \sqrt{1+2l}\frac{P_l^1(\cos\theta_m)\sin\theta_m}{l(l+1)}j_l(\rho R_i)Y_l^0(\theta,\phi)\Bigg]. \tag{A1}$$

When convolved with other charge distributions and the interaction potential, we get

$$U_{ij} = \sum_{L,M} 8i^{L-l_i-l_j}Y_L^M(\theta,\phi)\sum_{l_i,m_i,l_j,m_j}\mathcal{D}_{l_i}^{m_i}(\hat{R}_i)\mathcal{D}_{l_j}^{m_j}(\hat{R}_j) \times \mathcal{C}_{l_i,l_i,0}^{m_i,m_i,0}\mathcal{C}_{L,l_i,l_j}^{m_i,m_j}8\pi^{3/2}c_{l_i}c_{l_j}\mathcal{I}_{L,l_i,l_j}, \tag{A2}$$

where $\mathcal{I}$ is an integral defined by

$$\mathcal{I}_{L,l_i,l_j} = \int_0^\infty j_{l_j}(\rho R_j)j_{l_i}(\rho R_i)\frac{\rho^2}{\rho^2+\lambda^{-2}}j_L(\rho r)d\rho. \tag{A3}$$

To the best of our knowledge, this integral only has a known solution for $r > R_i + R_j$ and $\lambda = \infty$. Physically, this is two finite-size multipoles without any overlap between their charge distributions for unscreened electrostatic interactions. In this specific case, the integral can be written as [42]

$$\mathcal{I}_{L,l_i,l_j} = \frac{\pi^{3/2}}{2^3}\frac{R^{l_i+l_j}r^{-1-l_i-l_j}\Gamma\left(\frac{1+l_i+l_j+L}{2}\right)}{\Gamma(l_i+3/2)\Gamma(l_j+3/2)\Gamma\left(1+\frac{L-l_i-l_j}{2}\right)}F_4\left(\frac{l_i+l_j-L}{2},\frac{1+l_i+l_j+L}{2};l_i+\frac{3}{2},l_j+\frac{3}{2};\frac{R_i^2}{r^2},\frac{R_j^2}{r^2}\right), \tag{A4}$$

where F_4 is the Appell hypergeometric function of the fourth kind. Due to $\Gamma[1+(L-l_i-l_j)/2]$ in the denominator and the Clebsch-Gordan coefficient of (A2), it is only evaluated when $L = l_i + l_j$.

To see this, consider that $\max_L = l_i + l_j$, for which the Clebsch-Gordan coefficient is nonzero and the integral coefficient is nonzero. For $L = l_i + l_j - (2n+1)$, $n \in \mathbb{N}$, the symmetries are incompatible and the Clebsch-Gordan coefficient is zero. For $L = l_i + l_j - (2n)$, $n \in \mathbb{N}$, the Gamma function evaluates to a negative integer, which is a pole of the function.

Since the first coefficient of the function is zero, it is trivial $F_4(0,\beta;\gamma,\gamma';x,y) = 1$, yielding the usual powers of r for multipole expensions. For instance, the $L = l_i = l_j = 0$ contribution, which is the monopole-monopole term, yields the usual

$$U_{ij}^{L=l_i=l_j=0} = \frac{Q_iQ_j}{r}, \tag{A5}$$

where $Q_i = -4\pi R_i^2\cos\theta_m$. Note that we defined the energy between charges to be q_iq_j/r in $\chi_{\text{es}}(r)$, so this result is consistent with the unit system used $4\pi\epsilon = 1$.

APPENDIX B: FIELD EQUATIONS FROM STRETCHED EXPONENTIAL FUNCTIONS

In Eq. (3), we have defined the auxiliary field as an convolution between the pairwise interaction $\chi(r)$ and the density field $\rho_j(\vec{r})$. In Eq. (5), we relate the total energy to the convolution of the auxiliary field with the density field $\rho_i(\vec{r})$, which is written as

$$U_{ij}(\vec{r}_{ij},\hat{R}_i,\hat{R}_j) = \rho_i(\vec{r},\hat{R}_i) * \chi(r) * \underline{\rho_j}(\vec{r},\hat{R}_j). \tag{B1}$$

This triple convolution is then related to products in reciprocal space,

$$\tilde{U}_{ij}(\vec{\rho},\hat{R}_i,\hat{R}_j) = \tilde{\rho}_i(\vec{\rho},\hat{R}_i)\tilde{\chi}(\rho)\underline{\tilde{\rho}_j}(\vec{\rho},\hat{R}_j) = (\tilde{\rho}_i(\vec{\rho},\hat{R}_i)\tilde{\chi}(\rho)^{1/2})(\tilde{\chi}(\rho)^{1/2}\underline{\tilde{\rho}_j}(\vec{\rho},\hat{R}_j)). \tag{B2}$$

If there exists a well-defined inverse transform of $\tilde{\chi}^{1/2}(\rho)$ and assuming that $\rho_i(\vec{r}) = \rho_j(\vec{r})$, then we can define an new auxiliary field such that $\tilde{\Phi}_{\rho_i\chi}(\vec{\rho},\hat{R}_i) = \tilde{\rho}_i(\vec{\rho},\hat{R}_i)\tilde{\chi}(\rho)^{1/2}$. The energy is then defined as a self-convolution,

$$U_{ij} = \Phi_{\rho_i\chi}(\vec{r}_i,\hat{R}_i) * \underline{\Phi_{\rho_i\chi}}(\vec{r}_j,\hat{R}_j). \tag{B3}$$

The well-definedness of inverting $\tilde{\chi}(\rho)^{1/2}$ is quite limiting as we have only found that stretched exponentials $\chi(r) = \exp(-r^q)$ with $1/2 \leqslant q \leqslant 2$ fit this criteria.

APPENDIX C: VECTOR FIELDS

In Sec. II we describe directional interactions under the assumption that energy can be expressed as an overlap of scalar fields. However, the approach is generalizable to tensor fields. For simplicity, let us look at an interaction that stems from the inner product of the vector field of two distinct particles Φ_i and Φ_j,

$$U_{ij} = \int_V \vec{\Phi}_i\cdot\vec{\Phi}_j dV. \tag{C1}$$

This type of interaction can be used to describe electrostatic interactions through electric fields,

$$U_{ij}^E = \frac{1}{2}\int_V \epsilon|E|^2dV = \frac{1}{2}\int_V \epsilon(|E_i|^2+|E_j|^2+2\vec{E}_i\cdot\vec{E}_j)dV, \tag{C2}$$

where the first two terms are constants and the last term is in the same form as Eq. (C1). In order to evaluate (C1), we

separate the field into multiple components such that

$$\vec{\Phi}_i = \Phi^x \hat{x} + \Phi^y \hat{y} + \Phi^z \hat{z}. \tag{C3}$$

in the reference frame of the particle. The additional difficulty stems from the fact that once the particle is rotated, Φ^z may now point in the $\hat{x}$ direction. This is resolved by considering the overlap of nine fields, by taking rotation of unit vectors

$$U_{ij} = \sum_{k,k'} \int_V \Phi_i^k \Phi_j^{k'} \hat{R}_i \hat{k} \cdot \hat{R}_j \hat{k}' dV, \tag{C4}$$

where $k,k' = x,y,z$ and $\hat{R}_i$ is the rotation operator of the ith particle. Unlike the expansion done for interacting charges in Eq. (22), direct use of an electric field permits the use of charge distributions interacting in nonisotropic media, that is, ϵ only has the restriction that it needs to be constant throughout the volume. This could be used, for instance, to calculate charge interactions of colloids suspended in liquid crystal media, where ϵ is a tensor.

APPENDIX D: EXCLUDED VOLUMES AND VAN DER WAALS GAS

In coarse-grained models, one generally uses Lennard-Jones forces to model interactions. This includes a short-ranged repulsive part which shows a r^{-12} dependence. This would suggest use of $\chi(r) \sim (\sigma/r)^{12} - (\sigma/r)^6$. However, the Fourier transform of such a function does not exist. One could regularize it by changing r to $r + \delta$ or adding other short-ranged potentials to remove the divergence, but this hides a major problem in that we truncate the Fourier series or, equivalently, use spatial filtering. While Eq. (3) is strictly physical and exact, after truncation it is akin to

$$U_{ij} = \int_V \langle \rho_i(\vec{r}) \rangle \langle \Phi_{\rho_j}(\vec{r}) \rangle, \tag{D1}$$

where $\langle\rangle$ is some kind of spatial average consistent with the Fourier series truncation. If one plots the pair distribution function for a Lennard-Jones system, then it becomes trivial to see that no overlap is present for small values of r [or large $\chi(r)$]. In order to evaluate the excluded volumes, we will need

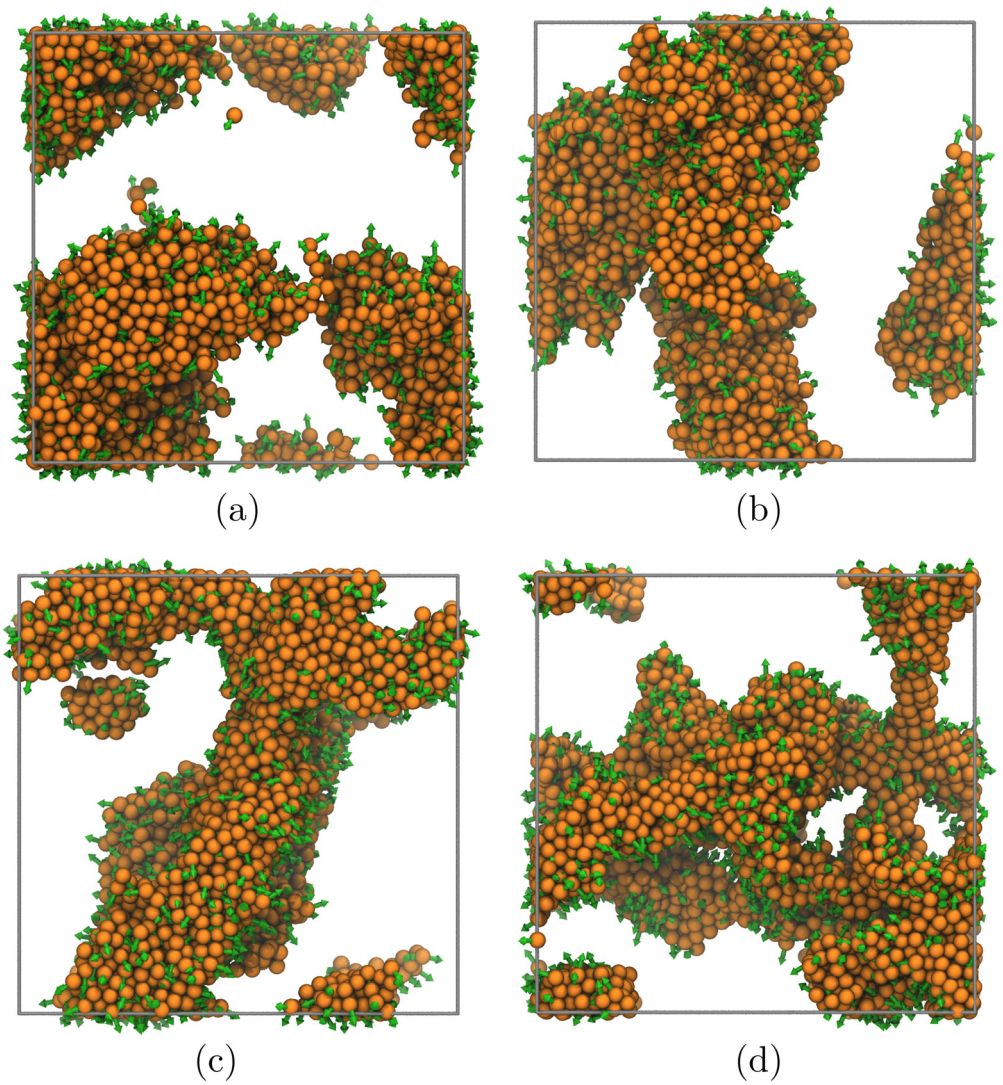

FIG. 6. Snapshots of the simulations of charged Janus particles ($\theta_m = 1.40$) for different temperatures: (a) $T = 1.62$, (b) $T = 1.42$, (c) $T = 1.20$, (d) $T = 1.0$. Arrows indicate the north pole of the Janus particles.

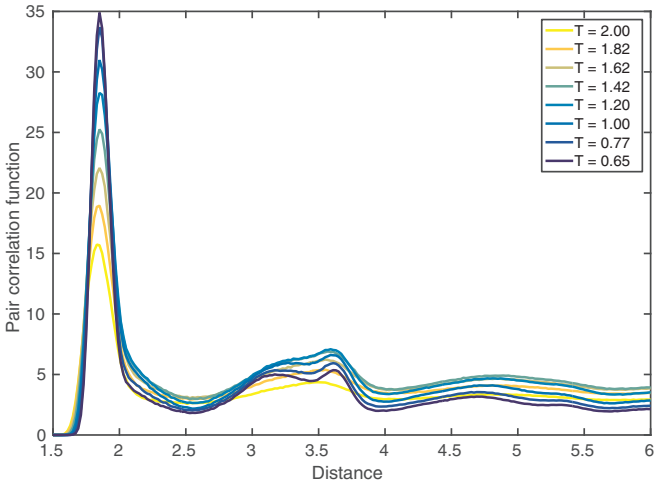

FIG. 7. Pair correlation functions for different temperatures for the asymmetric ($\theta_m = 1.40$) Janus particles for $\lambda = 0.32$.

to use some spatial average of the Lennard-Jones interactions. As an approximation, one can still use regularization, but it has to be done carefully as it may impact the system behavior.

Instead of using a soft repulsive term, one can start with the Van der Walls equation of state, which writes the average enthalpy per particle of a gas of hard spheres of volume b as

$$H_{\mathrm{VdW}}/N = k_B T\left(\frac{1}{1-\rho b} + \frac{3}{2}\right). \tag{D2}$$

Here we assume that we can treat all excluded volume interactions as Van der Waals gas and write the overall energy as the integral of the spatially filtered enthalpy. We also assume that local density can be written as pairwise densities, such that $\rho = \rho_i + \rho_j$ in the local enthalpy. Disregarding the constant $3/2$ term, this leads to a local enthalpy defined by

$$H_{\mathrm{VdW}}^{\mathrm{local}} = k_B T \frac{1}{1-(\rho_i+\rho_j)b}. \tag{D3}$$

In the present formalism, we cannot treat arbitrary potential in ρ. However, we can expand in power series,

$$\begin{aligned} H_{\mathrm{VdW}}^{\mathrm{local}} \approx k_B T[1 &+ b(\rho_i+\rho_j) + b^2(\rho_i+\rho_j)^2 \\ &+ b^3(\rho_i+\rho_j)^3 + \cdots]. \end{aligned} \tag{D4}$$

Given that powers of strictly ρ_i and ρ_j are not part of pairwise potentials of colloid, we do not have to deal with them. We are then left with the following interaction:

$$\begin{aligned} \beta H_{\mathrm{VdW}} = 2b^2 &\int_V \rho_i(\vec{r}-\vec{r}_i,\hat{R}_i)\rho_j(\vec{r}-\vec{r}_j,\hat{R}_j) \\ &+ 3b^3 \int_V \rho_i^2(\vec{r}-\vec{r}_i,\hat{R}_i)\rho_j(\vec{r}-\vec{r}_j,\hat{R}_j) \\ &+ \rho_i(\vec{r}-\vec{r}_i,\hat{R}_i)\rho_j^2(\vec{r}-\vec{r}_j,\hat{R}_j) + \cdots \end{aligned} \tag{D5}$$

One can then produce fields for $\rho(\vec{r},\hat{R})$, $\rho^2(\vec{r},\hat{R}),\ldots,$ for all colloids and truncate the series at some power of ρ.

APPENDIX E: SUPPLEMENTARY DATA FOR THE LIQUID-GEL TRANSITION

The liquid-gel morphology transition of asymmetric charged Janus particles is in appearance a continuous transition where the branches of the gel are thick near the liquid phase. This can be seen in Fig. 6. The transition is characterized by gradual changes of the pair correlation function, as shown in Fig. 7.

[1] F. Sciortino, A. Giacometti, and G. Pastore, Phys. Rev. Lett. **103**, 237801 (2009).
[2] Q. Chen, S. C. Bae, and S. Granick, Nature **469**, 381 (2011).
[3] J. Zhang, B. A. Grzybowski, and S. Granick, Langmuir **33**, 6964 (2017).
[4] J. Yan, M. Han, J. Zhang, C. Xu, E. Luijten, and S. Granick, Nat. Mater. **15**, 1095 (2016).
[5] M. Han, J. Yan, S. Granick, and E. Luijten, Proc. Natl. Acad. Sci. USA **114**, 7513 (2017).
[6] S. Sacanna, M. Korpics, K. Rodriguez, L. Colón-Meléndez, S.-H. Kim, D. J. Pine, and G.-R. Yi, Nat. Commun. **4**, 1688 (2013).
[7] X. Zheng, M. Liu, M. He, D. J. Pine, and M. Weck, Angew. Chem., Int. Ed. **129**, 5599 (2017).
[8] H. R. Vutukuri, A. Imhof, and A. van Blaaderen, Angew. Chem., Int. Ed. **53**, 13830 (2014).
[9] M. N. O'Brien, M. Girard, H.-X. Lin, J. A. Millan, M. O. de la Cruz, B. Lee, and C. A. Mirkin, Proc. Natl. Acad. Sci. USA **113**, 10485 (2016).
[10] S. Mann, Nat. Mater. **8**, 781 (2009).
[11] J. J. McManus, P. Charbonneau, E. Zaccarelli, and N. Asherie, Curr. Opin. Colloid Interface Sci. **22**, 73 (2016).
[12] E. Lindahl and M. S. P. Sansom, Curr. Opin. Struct. Biol. **18**, 425 (2008).
[13] M. X. Wang, J. D. Brodin, J. A. Millan, S. E. Seo, M. Girard, M. O. de la Cruz, B. Lee, and C. A. Mirkin, Nano Lett. **17**, 5126 (2017).
[14] U. Agarwal and F. A. Escobedo, Nat. Mater. **10**, 230 (2011).
[15] S. Torquato and Y. Jiao, Nature **460**, 876 (2009).
[16] J. de Graaf, R. van Roij, and M. Dijkstra, Phys. Rev. Lett. **107**, 155501 (2011).
[17] P. F. Damasceno, M. Engel, and S. C. Glotzer, Science **337**, 453 (2012).
[18] J. Downs, K. Gubbins, S. Murad, and C. Gray, Mol. Phys. **37**, 129 (1979).
[19] R. A. Sack, J. Math. Phys. **8**, 1774 (1967).
[20] K. Ruedenberg, Theor. Chim. Acta **7**, 359 (1967).
[21] J. G. Gay and B. J. Berne, J. Chem. Phys. **74**, 3316 (1981).
[22] D. J. Cleaver, C. M. Care, M. P. Allen, and M. P. Neal, Phys. Rev. E **54**, 559 (1996).
[23] D. J. Ashton, R. L. Jack, and N. B. Wilding, Soft Matter **9**, 9661 (2013).
[24] D. Marx and J. Hutter, *Ab initio* molecular dynamics: Theory and Implementation, *Modern Methods and Algorithms of Quantum*

Chemistry, edited by J. Grotendorst, NIC Series, Vol. 1 (John von Neumann Institute for Computing, Jülich, 2000), pp. 301–449.
[25] S. J. Plimpton, J. Comp. Phys. **117**, 1 (1995).
[26] See Supplemental Material at http://link.aps.org/supplemental/10.1103/PhysRevE.96.053309 for the LAMMPS implementation of the uniaxial case.
[27] W. Kung and M. O. de la Cruz, J. Chem. Phys. **127**, 244907 (2007).
[28] W. Kung, P. Gonzalez-Mozuelos, and M. O. de la Cruz, J. Chem. Phys. **133**, 074704 (2010).
[29] Z.-G. Wang, Phys. Rev. E **81**, 021501 (2010).
[30] J. M. Dempster and M. O. de la Cruz, ACS Nano **10**, 5909 (2016).
[31] N. Baddour, J. Opt. Soc. Am. A **27**, 2144 (2010).
[32] M. Boyle, Phys. Rev. D **87**, 104006 (2013).
[33] M. Toyoda and T. Ozaki, Comput. Phys. Commun. **181**, 277 (2010).
[34] B. Keinert, M. Innmann, M. Sänger, and M. Stamminger, ACM Trans. Graph. **34**, 193 (2015).
[35] R. Kjellander and R. Ramirez, J. Phys.: Condens. Matter **20**, 494209 (2008).
[36] W. M. Brown, T. D. Nguyen, M. Fuentes-Cabrerab, J. D. Fowlkes, P. D. Rack, M. Berger, and A. S. Bland, Proc. Comput. Sci. **9**, 186 (2012).
[37] J. C. Shelley and G. N. Patey, J. Chem. Phys. **103**, 8299 (1995).
[38] M. E. van Leeuwen and B. Smit, Phys. Rev. Lett. **71**, 3991 (1993).
[39] R. Agrawal and D. A. Kofke, Mol. Phys. **85**, 23 (1995).
[40] A. Travesset, Soft Matter **13**, 147 (2017).
[41] Y. Levin, P. S. Kuhn, and M. C. Barbosa, Physica A **292**, 129 (2001).
[42] I. S. Gradshteyn and I. M. Ryzhik, *Table of Integrals, Series, and Products*, 7th ed. (Elsevier/Academic Press, Amsterdam, 2007).